Research paper

Enhanced photocatalytic activity induced by sp³ to sp² transition of carbon dopants in BiOCl crystals

Jianguo Sun[a], Sujuan Wu[a,b,*], Shi-Ze Yang[b], Qi Li[a], Jiawei Xiong[a], Zhenzhong Yang[c], Lin Gu[c], Xixiang Zhang[d], Lidong Sun[a,*]

[a] Electron Microscopy Center of Chongqing University, College of Materials Science and Engineering, Chongqing University, Chongqing, 400044, China
[b] Materials Science and Technology Division, Oak Ridge National Laboratory, Oak Ridge, TN, 37831, USA
[c] Beijing National Laboratory for Condensed Matter Physics, Institute of Physics, Chinese Academy of Sciences, Beijing, 100190, China
[d] King Abdullah University of Science and Technology (KAUST), Division of Physical Science and Engineering, Thuwal, 23955-6900, Saudi Arabia

ARTICLE INFO

ABSTRACT

The insufficient light absorption and low quantum efficiency limit the photocatalytic performance of wide bandgap semiconductors. Here, we report a facile strategy to engineer the surface disordered defects of BiOCl nanosheets via carbon doping. The surface defects boost the light absorption and also the quantum yields, as the doped carbon atoms exhibit a transition from sp³ to sp² hybridization at elevated temperature, corresponding to a change of assembly state from 3D cluster to 2D graphite-like structure. This transition results in an effective charge separation and thus one order of enhancement in photocatalytic activity toward phenol degradation under visible light. The current study opens an avenue to introduce sp³ to sp² transition of carbon dopants for simultaneous increment of light absorption and quantum efficiency for application in photocatalysis and energy conversion.

1. Introduction

An efficient photocatalytic activity is dominated, to a large extent, by the light harvesting ability and charge separation process in a semiconductor [1]. Bismuth oxychloride (BiOCl) nanocrystals with layered structure exhibit impressive photocatalytic performance and hence attract extensive attention in the past decade [2–5]. Nevertheless, the photocatalysis can only be driven by ultraviolet light because of the large bandgap energy (E_g = 3.45 eV for intrinsic BiOCl [6]). As such, enormous efforts have been devoted to narrowing the bandgap energy by doping metal [7,8] or nonmetal [9,10] impurities for improved light harvesting. This usually extends the light response into the visible region with enhanced photocatalytic activity [11–15]. However, it is on the other hand still limited by the charge separation process. Considering the layered structure of BiOCl crystals and the established electric field within each single layer, doping would be possible to maintain the electric field within each layer meanwhile enhance the electronic coupling between the layers. This in turn gives rise to narrowed bandgap energy and promoted charge separation simultaneously. Besides, surface defects engineering is an effective strategy to tune the surface states that affect the charge separation during the photocatalysis [1,16]. The surface states can trap the

photogenerated electrons or holes and thus suppress the recombination. This yields intriguing photocatalytic performance [17,18]. Therefore, engineering the surface disordered defects in a good manner is capable of enhancing the light absorption and meanwhile facilitating the charge separation for efficient photocatalysis.

In this study, surface disorders are introduced into bismuth oxychloride nanosheets by glucose treatment. Both the experimental results and density functional simulations indicate that surficial chlorine atoms are partially replaced by the carbon dopants (C_{Cl}). The resulting BiOCl nanosheets exhibit strong visible light absorption and significantly enhanced photocatalytic activity toward phenol degradation. Moreover, it is found that the transition from sp³ to sp² hybridization of the carbon dopants arises at elevated temperature, resulting in further improvement of the photocatalytic activity. These findings pave ways for developing efficient photocatalysts by engineering the surface disordered defects.

2. Experimental

2.1. Preparation of C-BiOCl powders

All of the reagents were analytical grade without further

* Corresponding authors at: Electron Microscopy Center of Chongqing University, College of Materials Science and Engineering, Chongqing University, Chongqing, 400044, China.
E-mail addresses: sujuan.wu@cqu.edu.cn (S. Wu), lidong.sun@cqu.edu.cn (L. Sun).

purification. 5 g Bi_2O_3 was dissolved in 20 mL 37% hydrochloric acid under vigorous stirring for 5 min. Then, the solution was evaporated at 350 °C, and white precipitates were obtained by adding 200 mL deionized water. Subsequently, the resulting precipitates were annealed at 400 °C for 4 h to acquire pure bismuth oxychloride powders. For carbon doping, the BiOCl powders and glucose were mixed with a mole ratio 7:5, and annealed at 160 °C, 180 °C, 200 °C and 220 °C under Ar (purity, 99.99%) protection. When the annealing temperature exceeded 220 °C, Bi metals were formed. Accordingly, the annealing temperature was controlled under 220 °C in this study. After washing with deionized water, the carbon-doped BiOCl (C-BiOCl) powders were attained. For comparison, the glucose alone was annealed at 220 °C under Ar protection to get carbon powders. The obtained carbon and BiOCl powders were mixed together with a mole ratio of 1:1, and then dispersed in alcohol by ultrasonicating for 30 min. The solution was left for 12 h to attain carbon adsorbed BiOCl (C@BiOCl) powders.

2.2. Characterization

X-ray diffraction (XRD) patterns were recorded by an Empryean X-ray diffractometer with monochromatic Cu K_α radiation ($\lambda = 1.5418$ Å). Scanning transmission electron microscopy (STEM) images were collected using an FEI Titan 80–300 Super Twin electron microscope operated at 200 kV and Nion Ultra STEM 200 with sub-Ångstrom resolution at 200 kV. Scanning electron microscopy (SEM) images and energy dispersive spectroscopy (EDS) were collected by using a field emission JEOL-SEM (JSM-7800F) equipped with energy spectrometer. X-ray photoelectron spectroscopy (XPS) measurements were carried out with the Thermo ESCALAB 250Xi system with Al Kα (hυ = 1486.6 eV) as the excitation source. Raman spectra were recorded in the region of 40–2000 cm^{-1} using a confocal Laser Micro-Raman Spectrometer (LabRAM HR Evolution) with a laser of 532 nm and 10 mW. The optical absorption spectra were measured from 240 to 800 nm using Shimadzu UV-2100 UV–vis spectrophotometer.

2.3. Photocatalytic measurements

The visible light driven photocatalytic activity was evaluated by photocatalytic degradation of 15 mg/L Phenol under 500 W Xe lamp with an ultraviolet cutoff filter ($\lambda > 420$ nm). In a typical process, 50 mg photocatalysts were dispersed into 100 mL and 15 mg/L phenol solution. Prior to illumination, the solution was continuously stirred for 1 h at 800 rpm in dark to establish the adsorption-desorption equilibrium. Then the concentration of phenol was measured to monitor the photocatalytic degradation by UV–vis Spectrophotometer (Shimadzu UV-2100).

2.4. Electrochemical measurements

The electrochemical experiments were carried out with a CHI 660E electrochemical system using a constructed three-electrode system. A Pt plate (0.5 × 0.5 cm^2) was used as a counter electrode and saturated calomel electrode was used as a reference electrode. As-prepared powders of 0.01 g were uniformly self-deposited onto an ITO glass with an area of 1.1 × 1.3 cm^2 and employed as the working electrode. The solution of 0.1 mol/L Na_2SO_4 was used as the electrolyte and a 500 W Xe lamp with a cutoff filter ($\lambda > 420$ nm) was utilized as the visible light source. Electrochemical impedance spectroscopy (EIS) measurements were carried out in the frequency between 1 Hz and 1 MHz in Na_2SO_4 (0.5 mol/L) solution, which was performed at an open circuit potential with 5 mV amplitude of the sinusoidal wave.

2.5. Computational methods

Density functional theory (DFT) calculations were performed using the projected augmented wave method (PAW) [19,20] as implemented in Vienna ab initio simulation package (VASP) [21,22]. For the structural relaxation and electronic structure calculations, generalized gradient approximation (GGA) method was used with Perdew-Burke-Ernzerhof (PBE) exchange-correlation functional [23]. The wave-plane cutoff energy was 520 eV and a regular Monkhorst-Pack grid of 6 × 6 × 4 points were used in all of the calculations. A 2 × 2 × 2 supercell was used in the simulation. The convergence criteria for structural optimization and energy on each atom were set to 0.01 eV/Å and 10^{-4} eV, respectively. A GGA + U method was adopted in calculation of density of states. The U values were set to 4.8 eV for the p-states of Bi and O, 7 eV for the p-states of Cl.

3. Results and discussion

3.1. Crystal structure analysis

BiOCl nanosheets with an average thickness of about 120 nm were prepared via hydrothermal method. The nanosheets were subsequently reduced through glucose treatment. Scanning electron microscopy images reveal that no obvious morphological changes appear after reduction of BiOCl (see Fig. S1 in the Supporting information). The incorporation of carbon atoms through glucose reduction is confirmed by the energy dispersive X-ray spectroscopy measurement (see Fig. S2 and Table S1 in the Supporting information), where the main compositions are Bi, O and Cl elements. To confirm the carbon doping, X-ray diffraction measurements were performed. Fig. S3 shows that the BiOCl nanosheets remain tetragonal structure (JCPDS No.85-0861) after glucose treatment, while no impurity phases (e.g., graphite) are observed. However, detailed observation (Fig. 1a–c) discloses that, upon glucose treatment, the (001) peak shifts to smaller angle, whereas the (200) and (104) peaks shift to larger angle as the annealing temperature increases. The shift of (001), (200), (104) peak is about 0.10°, 0.11°, 0.08°, respectively, which is much larger than the instrument error of about 0.02° (see Fig. S4 in the Spporting information). This demonstrates that the crystal lattice has an anisotropic distortion along different directions. The magnitude of lattice expansion is determined to be about 1% along the [001] direction. This is much smaller than ∼5% for a perfect intercalation of carbon dopants between the [Cl-Bi-O-Bi-Cl] units, as computed by simulations (see Fig. S5 in the Supporting information). Instead, it is consistent with the case that the C dopants substitute the Cl terminals, resulting in a distortion of ∼1.3%. This suggests that carbon atoms are doped into the BiOCl lattice by replacing partial of the Cl terminals in the [Cl-Bi-O-Bi-Cl] units.

Raman spectra were employed to further examine the microstructure of the carbon-doped BiOCl (C-BiOCl) crystals. Fig. 1d displays three characteristic peaks at 58.3, 142.6 and 199.5 cm^{-1} for each condition, which are assigned to the A_{1g} internal, the E_g external and internal Bi−Cl stretching modes in BiOCl crystals, respectively [24]. As the annealing temperature increases, the intensity of internal Bi−Cl stretching peak decreases and almost disappears at 220 °C, indicating the breaking of Bi−Cl bonds. This reveals that partial of the Cl atoms are removed during the reduction reaction, in good agreement with the substitution of Cl terminals with C dopants. More importantly, another four peaks at 1310, 1439, 1560 and 1654 cm^{-1} arise upon glucose treatment, as shown in Fig. 1e. The peaks at around 1310 and 1560 cm^{-1} are associated with the disordered (D-band) and graphitic carbon (G-band) [25], respectively. Red shifts up to ∼40 cm^{-1} and ∼20 cm^{-1} are observed for the D and G bands, as the annealing temperature increases. This can be attributed to the interactions between carbon atoms and BiOCl [26,27], in line with the lattice distortion observed by the peak shift in the XRD patterns. The band at 1654 cm^{-1} (D' band) originates from the vibrational mode induced by the formation of nano-crystalline or defect graphitic carbon [28,29]. The band at 1439 cm^{-1} is a special Raman-active phonon mode related to the vibrations of pentagonal rings in fullerenes [30]. In general, the formation of fullerenes requires either high temperature or ultrahigh pressure
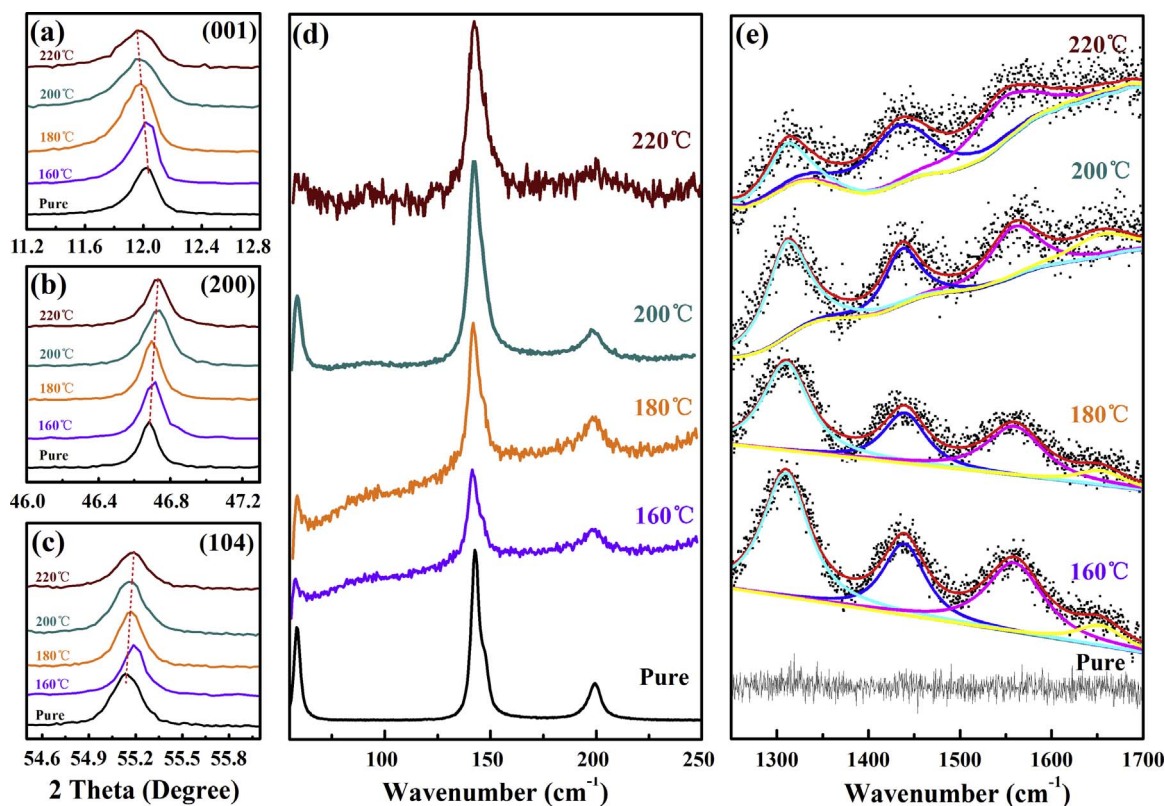
Fig. 1. Detailed XRD patterns of (001), (200) and (104) peaks (a–c) and corresponding Raman spectra (d-e) of pure and carbon-doped BiOCl powders prepared at different temperatures.

[31,32]. These two bands are usually absent in common graphene, graphite, and diamond-like carbon materials, while their presence herein implies the abnormal environment that the carbon atoms encounter. This could only be achieved by the constraint from the BiOCl lattice, echoing the structure that the carbon dopants replace the Cl terminals in the [Cl-Bi-O-Bi-Cl] unit and are thus confined between neighboring units. Besides, it is also found that the intensity of the peak ratio I_G/I_D exhibits a drastic increment between 180 and 220 °C, as is discussed later.

Chemical states of the BiOCl before and after glucose treatment were examined with X-ray photoelectron spectroscopy, as shown in Fig. 2. The C1s spectrum can be deconvolved into three peaks upon glucose treatment. The peak at 284.6 eV can be assigned to −C−C bands, while another two additional peaks at 287.3 eV and 286.1 eV are attributed to −C−O−C and −O−C bands, respectively [33,34]. The Bi4f spectrum can be deconvolved into two pairs of doublets, with those at 164.7 eV and 159.4 eV being ascribed to the Bi^{3+} in stoichiometric BiOCl. The emerging pairs at 164.2 eV and 158.9 eV are attributed to a lower chemical state of bismuth ions, which may originate from the

bonding between carbon and Bi [4,35]. This further supports the microstructure that partial of the chlorine terminals are replaced by carbon atoms because of doping. Considering the coordination feature of the Bi ions in a BiOCl bulk, where one Bi^{3+} ion is coordinated to four chlorine elements with a distance of 3.06 Å and four oxygen elements with a distance of 2.32 Å, the longer Bi−Cl bonds tend to break off and are thus replaced by Bi−C bonds. Fig. 2c reveals that the valence band maximum shifts from 2.44 eV to 1.75 eV upon doping. This agrees well with the calculated density of states for carbon-doped BiOCl (see Fig. S6 in the Supporting information). The carbon doping via replacing the chlorine terminals gives rise to defect levels near the valence band maximum, hence facilitating the hole transport in the BiOCl crystals.

Atomic-resolution high-angle annular dark field (HAADF) scanning transmission electron microscopy images show that the pure BiOCl nanosheets are well crystallized without any lattice distortion at both (001) and (010) facets, as displayed in Fig. 3a and b. In contrast, upon glucose treatment, the peripheral region of the (001) facets become disordered (Fig. 3c). However, the central region remains unchanged as evidenced by the same lattice spacing of 0.275 nm for both (100) and
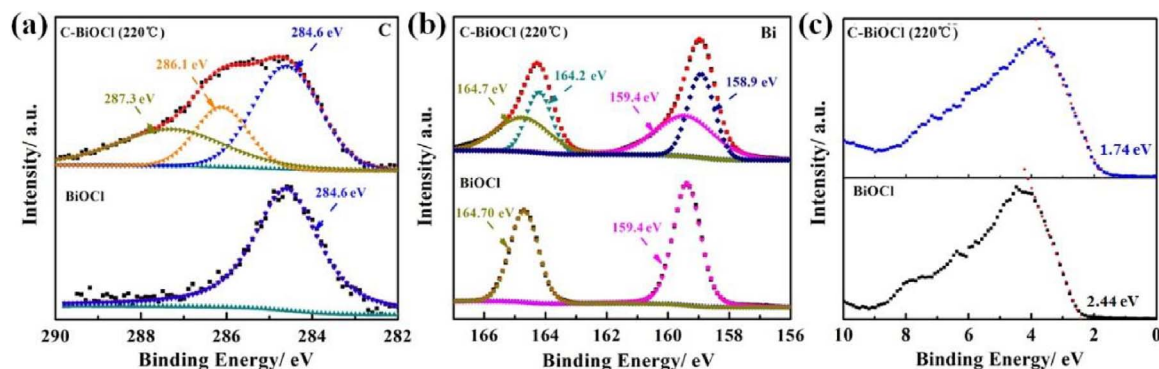

Fig. 2. X-ray photoelectron spectroscopy results of BiOCl and C-BiOCl annealed at 220 °C. (a) C 1 s core level, (b) Bi 4f core level, (c) valance band.
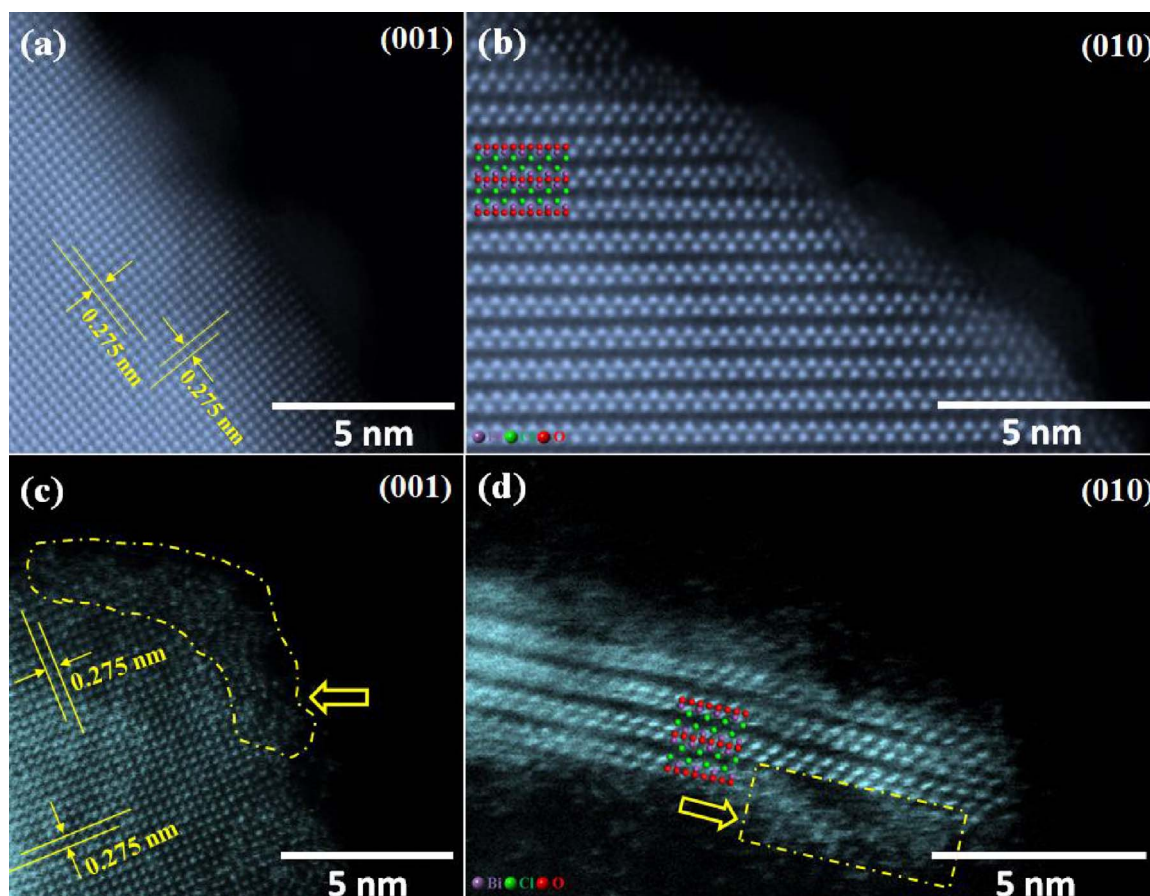
Fig. 3. Atomic-resolution HAADF-STEM images of the (001) (a, c) and (010) (b, d) facets for pure BiOCl (a, b) and C-BiOCl annealed at 220 °C (c, d).

(010) planes. Obvious distortion occurs at the (010) facets (Fig. 3d), where the outmost layers are almost destroyed, as a result of carbon doping. This indicates that surface disorders are introduced into the BiOCl crystals at the (010) facets via carbon doping. The dopants replace partial of the chlorine terminals in the [Cl-Bi-O-Bi-Cl] unit, and are thus confined between neighboring units. This induces the lattice expansion along the [001] direction (see XRD patterns in Fig. 1), the emerging Bi−Cl vibration modes because of lattice confinement (see Raman spectra in Fig. 1), and the binding energy shift toward lower end for Bi4f (see XPS spectra in Fig. 2). Such a doping incorporates defect levels close to valance band maximum, therefore narrowing the bandgap energy and facilitating charge separation as well as hole transport.

3.2. Visible light photocatalysis analysis

The photocatalytic property of the carbon-doped BiOCl is evaluated by degradation of colorless phenol under visible light illumination at $\lambda > 420$ nm. Fig. 4a shows that the pristine BiOCl exhibits negligible absorption in visible light region, because of the large bandgap. In contrast, substantial increment in absorption is achieved upon incorporating the surface disorders and carbon doping, which enhances with the treatment temperature. This is attributed to the narrowed bandgap energy from 2.99 to 2.26 eV (estimated based on Tauc plots in Fig. S7). Fig. 4b displays that a very small photocurrent of 0.2×10^{-7} A/cm^2 is produced with the pristine BiOCl, due to the limited absorption in visible region. The photocurrent is substantially enhanced upon carbon doping and increased gradually with elevated temperature. The C-BiOCl annealed at 220 °C exhibits the largest photocurrent of about 2.7×10^{-7} A/cm^2, an order of enhancement as compared to the pristine BiOCl. As a consequence, the pure BiOCl

renders no obvious degradation of phenol under visible light, while all of the carbon-doped BiOCl present impressive degradation rate under the same conditions, as compared in Fig. 4c and d. For comparison, control samples with carbon adsorbed onto the surface of BiOCl powders (referred to as C@BiOCl) were also prepared and used for degradation of phenol under the same conditions. Although the C@BiOCl exhibits similar absorption as the C-BiOCl annealed at 220 °C, it shows negligible photocatalytic degradation of phenol neither, this further verifies that the excellent visible light photocatalytic activity of C-BiOCl indeed originates from doped carbon atoms. Based on the previous reports, superoxide radicals (O$_2 \cdot^-$) and holes (h$^+$) from carbon doped BiOCl play a key role in such a photocatalytic process [12].

Very interestingly, about 40% of the phenol is degraded after 120 min using C-BiOCl powders annealed at 160 or 180 °C, whereas approximately 80% is achieved with those annealed at 200 or 220 °C, more than twice enhancement in the degradation rate. This is closely related to the I$_G$/I$_D$ ratio, which exhibits a dramatic increase between 180 and 220 °C (See Table 1). In general, the D-band corresponds to the breathing vibrations of sp^3 carbon, whereas the G-band is assigned to the in-plane vibrational motion of sp^2 carbon [30]. The increased ratio of I$_G$/I$_D$ demonstrates an abrupt increment in sp^2 content upon annealing at 200 or 220 °C, accompanied by the transition of carbon states from three-dimensional (3D) to two-dimensional (2D) assembly. In other words, the carbon dopants change from 3D clusters to 2D graphite-like structure above a critical temperature, driven by the high pressure imposed by the lattice confinement with the assistance of elevated temperature. Such an increase in sp^2 content provides more unsaturated π bonds, thus promoting the charge separation and facilitating the hole transport in BiOCl crystals during photocatalytic reactions. This is justified by the lower transfer resistance at BiOCl/electrolyte interface (see EIS results in Fig. S8) and higher photocurrent
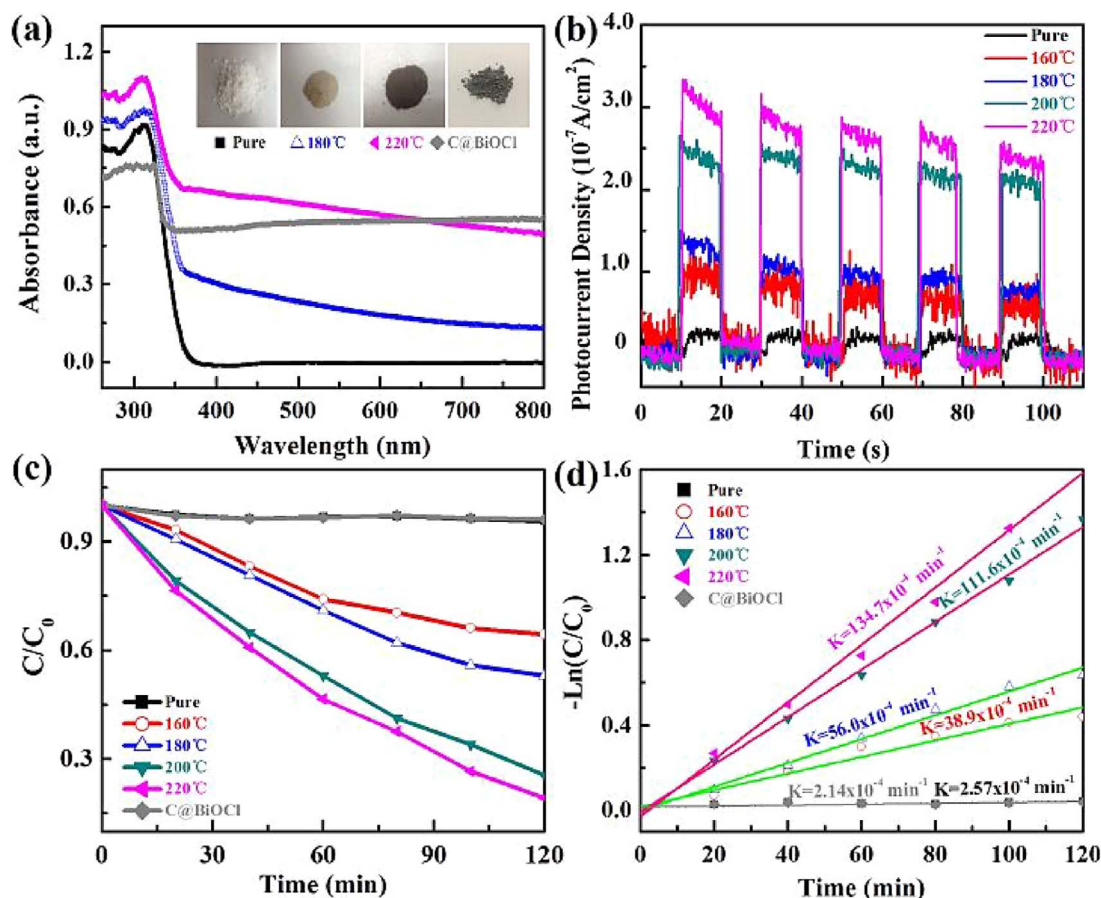
Fig. 4. UV–vis diffuse reflection spectra (a), transient photocurrent generation (b), photocatalytic degradation of phenol under visible light (c), and kinetic fit for phenol degradation under visible light illumination (d). Insets in (a) are corresponding photographs of different BiOCl powders.

Table 1
Raman peak intensity of D and G bands for C-BiOCl prepared at different temperatures.

	I_D	I_G	I_G/I_D
160 °C	1099.11	540.12	0.49
180 °C	1098.59	540.59	0.49
200 °C	212.18	248.93	1.17
220 °C	96.51	179.26	1.86

generation with high sp^2 content. According to the results obtained in this study, it is believed that, in principle, the photocatalytic activity of C-BiOCl will be enhanced when all of the sp^3 are completely converted to sp^2, as the sp^2 hybridization promotes the charge separation and facilitates the hole transport in the crystals. However, in practice further increment in I_G/I_D ratio is limited by the formation of bismuth (Bi) and bismuth oxides (Bi_2O_3) particles with elevated temperature above 220 °C, as shown in Fig. S9. As such, the highest I_G/I_D ratio of 1.86 is achieved at 220 °C with best photocatalytic performance in this study. Besides, it is also difficult to fully convert the sp^3 hybridization to sp^2, as the carbon atoms interact with the BiOCl crystals. This results in defects in the assembled sp^2 state, thus tends to exist as sp^3 hybridization state [36].

Based on the above results, the formation and transition process of carbon doping is illustrated in Fig. 5. In the process of glucose treatment, the glucose molecules are adsorbed on the BiOCl surface first, and the carbonaceous species block and stabilize the implanted carbon atoms. The lattice has a self-purification effect [37], resulting in doping only within the surface layer. With the increasing temperature, carbon atoms energetically prefer to substitute Cl terminals in each [Cl-Bi-O-Bi-Cl] unit, leading to the lattice expansion along the [001] direction.

Meanwhile, carbon dopants are confined between the [Cl-Bi-O-Bi-Cl] units, causing the transformation from sp^3 to sp^2 hybridization with the assistance of elevated temperature. Such a transition enhances the charge separation process and accelerates the hole transport, thus benefiting the photocatalytic activity.

4. Conclusion

In this study, surface disorders are introduced into BiOCl crystals by carbon doping at the (010) facets, where the chlorine terminals in each [Cl-Bi-O-Bi-Cl] are replaced by carbon dopants. Meanwhile, a transition from sp^3 to sp^2 hybridization occurs for the dopants at elevated temperature, corresponding to a transition of assembly state from 3D clusters to 2D graphite-like structure. This significantly increases the photocatalytic activity toward phenol degradation under visible light, i.e., from 38.9×10^{-4} to $134.7 \times 10^{-4} \, min^{-1}$. It is attributed to the enhanced visible light absorption and promoted charge separation. This study sheds light on manipulating the sp^2 transition of dopants for designing high performance semiconductors toward application in photocatalysis and energy conversion.
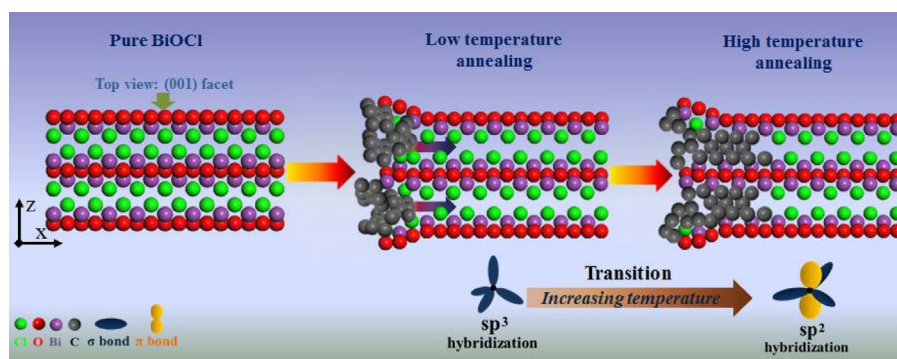
Fig. 5. Schematic illustration of the transition of carbon dopants from sp^3 to sp^2 hybridization in BiOCl crystal with elevated temperature.

Appendix A. Supplementary data

Supplementary data associated with this article can be found, in the online version, at http://dx.doi.org/10.1016/j.apcatb.2017.09.037

References

[1] X. Chen, L. Liu, Y.Y. Peter, S.S. Mao, Science 331 (2011) 746–750.
[2] K. Zhang, C. Liu, F. Huang, C. Zheng, W. Wang, Appl. Catal. B Environ. 68 (2006) 125–129.
[3] H. Cheng, B. Huang, Y. Dai, Nanoscale 6 (2014) 2009–2026.
[4] L. Ye, K. Deng, F. Xu, L. Tian, T. Peng, L. Zan, Phys. Chem. Chem. Phys. 14 (2012) 82–87.
[5] J. Jiang, K. Zhao, X. Xiao, L.Z. Zhang, J. Am. Chem. Soc. 134 (2012) 4473–4479.
[6] X. Liu, Y. Su, Q. Zhao, C. Du, Z. Liu, Sci. Rep. 6 (2016).
[7] F. Giordano, A. Abate, J.P.C. Baena, M. Saliba, T. Matsui, S.H. Im, M. Graetzel, Nat. Commun. 7 (2016).
[8] Y. Yang, X.L. Fan, R. Pan, W.J. Guo, Phys. Chem. Chem. Phys. 18 (2016) 10152–10157.
[9] X. Chen, C.J. Burda, Am. Chem. Soc. 130 (2008) 5018–5019.
[10] Y. Zheng, Y. Jiao, L. Ge, M. Jaroniec, S.Z. Qiao, Angew. Chem. Int. Ed. 125 (2013) 3192–3198.
[11] J. Yu, B. Wei, L. Zhu, H. Gao, W. Sun, L. Xu, Appl. Surf. Sci. 284 (2013) 497–502.
[12] J. Di, J. Xia, M. Ji, B. Wang, S. Yin, Q. Zhang, H. Li, ACS Appl. Mater. Interfaces 7 (2015) 20111–20123.
[13] J. Xia, L. Xu, J. Zhang, S. Yin, H. Li, H. Xu, J. Di, Cryst. Eng. Comm. 15 (2013) 10132–10141.
[14] Z. Jiang, Y. Liu, T. Jing, B. Huang, Z. Wang, X. Zhang, Y. Dai, RSC Adv. 5 (2015) 47261–47264.
[15] J. Li, K. Zhao, Y. Yu, L.Z. Zhang, Adv. Funct. Mater. 25 (2015) 2189–2201.
[16] X. Yu, B. Kim, Y.K. Kim, ACS Catal. 3 (2013) 2479–2486.
[17] X. Chen, L. Liu, Z. Liu, M.A. Marcus, W.C. Wang, N.A. Oyler, J. Guo, Sci. Rep. 3 (2013) 1510.
[18] J. Lu, Y. Dai, H. Jin, B. Huang, Phys. Chem. Chem. Phys. 3 (2011) 18063–18068.
[19] P.E. Blöchl, Phys. Rev. B 50 (1994) 17953.
[20] G. Kresse, D. Joubert, Phys. Rev. B 59 (1990) 1758.
[21] G. Kresse, J. Furthmüller, Comput. Mater. Sci. 6 (1996) 15–50.
[22] G. Kresse, J. Furthmüller, Phys. Rev. B 54 (1996) 11169.
[23] J.P. Perdew, K. Burke, M. Ernzerhof, Phys. Rev. Lett. 77 (1996) 3865.
[24] J.E.D. Davies, J. Inorg. Nucl. Chem. 35 (1973) 1531–1534.
[25] A.C. Ferrari, J.C. Meyer, V. Scardaci, C. Casiraghi, M. Lazzeri, F. Mauri, A.K. Geim, Phys. Rev. Lett. 97 (2006) 187401.
[26] M. Huang, H. Yan, T.F. Heinz, J. Hone, Nano Lett. 10 (2010) 4074–4079.
[27] L. Gong, I.A. Kinloch, R.J. Young, I. Riaz, R. Jalil, K.S. Novoselov, Adv. Mater. 22 (2010) 2694–2697.
[28] R.J. Nemannich, Phys. Rev. B 20 (1979) 392–420.
[29] M.H. Oliveira, T. Schumann, R. Gargallo-Caballero, F. Fromm, T. Seyller, M. Ramsteiner, A. Trampert, L. Geelhaar, J.M.J. Lopes, H. Riechert, Carbon 56 (2013) 339–350.
[30] R. Saito, M. Hofmann, G. Dresselhaus, A. Jorio, M.S. Dresselhaus, Adv. Phys. 60 (2011) 413–550.
[31] V.D. Blank, V.N. Denisov, A.N. Kirichenko, B.A. Kulnitskiy, S.Y. Martushov, B.N. Mavrin, I.A. Perezhogin, Nanotechnology 18 (2007) 345601.
[32] D.W. Lau, D.G. McCulloch, N.A. Marks, N.R. Madsen, A.V. Rode, Phys. Rev. B 75 (2007) 233408.
[33] O. Akhavan, E. Ghaderi, S. Aghayee, Y. Fereydooni, A.J. Talebi, Mater. Chem. 22 (2012) 13773–13781.
[34] C. Xu, X. Wang, J.J. Zhu, Phys. Chem. C 112 (2008) 19841–19845.
[35] Y. Yu, C. Cao, H. Liu, P. Li, F. Wei, Y. Jiang, W.J. Song, Mater. Chem. A 2 (2014) 1677–1681.
[36] L.G. Cançado, A. Jorio, E.H. Martins Ferreira, F. Stavale, C.A. Achete, R.B. Capaz, M.V.O. Moutinho, A. Lombardo, T.S. Kulmala, A.C. Ferrari, Nano Lett. 11 (2011) 3190–3196.
[37] D. Chen, R. Viswanatha, G.L. Ong, R. Xie, M. Balasubramaninan, X. Peng, J. Am. Chem. Soc. 131 (2009) 9333–9339.